J Eng Math (2009) 63:135–151
DOI 10.1007/s10665-008-9253-z

Axisymmetric flow of two fluids in a pulsating pipe

Y. Li · M. G. Blyth

Received: 23 January 2008 / Accepted: 13 October 2008 / Published online: 31 October 2008

Abstract The motion of a viscous thread surrounded by an annular viscous layer inside a pulsating cylindrical pipe whose radius is a periodic function of time is investigated. At zero Reynolds number, a stagnation-point-type solution may be written down in closed form. A Floquet linear stability analysis for Stokes flow reveals the pulsations either decrease or increase the growth rate of longwave disturbances depending on the initial radius of the thread. For a moderate-sized initial thread radius, increasing the amplitude of the pulsations decreases the critical wavenumber for instability to below the classical Rayleigh threshold. Increasing the viscosity contrast, so that the fluid in the annular layer becomes more viscous than the fluid in the thread, tends to decrease the growth rate of disturbances. In the second part of the paper, the basic stagnation-point-type flow at arbitrary Reynolds number is computed using a numerical method on the assumption that the interface is a circular cylinder at all times. During the motion, either the thread radius tends to increase and the thickness of the annular layer decreases, or else the thread tends to thin and the thickness of the annular layer increases, depending upon the initial conditions and the parameter values. For a judicious choice of initial condition, a time-periodic exact solution of the Navier–Stokes equations is identified.

Keywords Interfacial flow · Navier–Stokes flow · Stokes flow

1 Introduction

Pulsating flows involving two or more fluid constituents arise in a number of biological applications. In the human digestive tract, liquid and solid meals arriving in the fundus, the upper part of the stomach, are slowly mixed with enzymes through a gentle pulsing of the stomach wall (e.g. [1]). The enzymes can be treated as a layer of viscous fluid which, upon secretion, coat the inside of the gastric wall and surround the core fluid meal before convecting and diffusing into the interior. In healthy human lungs, the thin layer of liquid mucus coating the inside of the airways decreases in thickness during expiration (e.g. [2]). During normal rhythmic breathing, closure of the smaller airways may occur due to the formation of a liquid mucus lens, or through the closure of the compliant elastic airway wall, or through a combination of these two effects. Monitoring the occurence of closure is one means of determining healthy lung function (e.g. [3]).

Y. Li · M. G. Blyth (✉)
School of Mathematics, University of East Anglia, Norwich NR4 7TJ, England, UK
e-mail: m.blyth@uea.ac.uk

Motivated by examples such as these, in the present paper we undertake a general theoretical investigation of the effect of wall pulsations on an axisymmetric arrangement of two fluids in a cylindrical pipe.

Lord Rayleigh [4, 5] investigated the stability of a quiescent inviscid or viscous liquid thread suspended *in vacuum*. When the wavelength of an axisymmetric perturbation is larger than the circumference, the thread is unstable and disintegrates into a file of liquid drops (e.g. [6]). The more general scenario with a viscous thread at rest inside an ambient viscous fluid was studied by Weber [7] and Tomotika [8], who identified the same critical wavelength for instability and calculated the wavelength of the most rapidly growing disturbance. Goren [9] discussed the stability of a quiescent liquid film coating a straight wire or wetting the inside of a hollow cylindrical tube, and computed the wavelength of the most dangerous disturbance. Hammond [10] studied the nonlinear evolution of a thin annular film, which surrounds a cylindrical viscous thread and coats the inside of a circular cylinder, and showed that the film is unstable to longwave disturbances which break up the fluid film into disconnected lobes. More recently, Kwak and Pozrikidis [11] extended Tomotika's analysis to allow for the presence of confining walls and, in particular, to include the effect of an insoluble surfactant at the interface between the fluids.

Tomotika [12] examined the stability of a viscous thread undergoing extensional flow inside a surrounding viscous fluid. His analysis was improved upon by Mikami et al. [13], who also compared their results with experiments. The intriguing feature of this problem is the competition between the stabilising action of the extensional flow, which tends to oppose the growth of interfacial disturbances, and the capillary instability which comes into play as the wavelength of a disturbance is stretched by the flow beyond the critical Rayleigh limit. Mikami et al. [13] showed that under most conditions an initial disturbance may go through a transitory period of growth due to the capillary instability, but ultimately it decays and the thread is stabilised. This observation was confirmed by Kwak et al. [14], who also accounted for the presence of an insoluble surfactant and compared the results of the linear theory at zero Reynolds number with full boundary-integral simulations of the equations of Stokes flow. Khakhar and Ottino [15] considered the evolution of a viscous thread in an arbitrary linear flow and found results which are in broad agreement with the results for axisymmetric flow.

As noted above, the convective effect of an extensional flow is to lower the amplitude of small disturbances while stretching their wavelength into the regime where they fall prey to the Rayleigh instability. Presumably, if the direction of flow is reversed, convection will tend to amplify linear disturbances but at the same time shorten their wavelength and reduce the chance of the Rayleigh instability. This raises the interesting question of how the thread behaves if the flow is oscillating in time, so that the flow direction reverses every half period. The stability of multi-component axisymmetric oscillating fluid systems has been discussed by a number of authors. For example, Halpern and Grotberg [16] studied the case of a thin viscous film on the inside of a cylindrical pipe surrounding a core fluid undergoing oscillating flow. Blyth and Pozrikidis [17] examined the stability of a pulsating gas column inside either an inviscid or a viscous fluid at zero Reynolds number using Floquet analysis. Of particular relevance to the present work is the two-dimensional study by Blyth [18], which considered the effect of pulsations on the stability of two-layer flow in a channel. Blyth showed that the pulsations tend to raise the growth rate of normal modes, but are unable to destabilise an otherwise stable configuration.

In this paper, we investigate the behaviour of a viscous thread surrounded by an annular viscous layer inside a pulsating cylinder whose radius varies periodically in time. The axisymmetric flow is assumed to adopt a stagnation-point-type structure where the axial component of velocity is proportional to distance along the axis, and the radial component of velocity is independent of the axial coordinate. In the basic configuration, the motion of the wall induces an alternately extensional and contracting flow for which the interface between the two fluids is a circular cylinder at all times. Under these stipulations, an exact solution valid at zero Reynolds number may be written down in closed form. Since the basic flow is periodic in time, we can use Floquet theory to study the development of a linear interfacial disturbance, and compute the growth rates of normal modes. In the second part of the paper, we study the motion of the thread at arbitrary Reynolds number. The flow is again assumed to adopt a stagnation-point-type structure, with a linear dependence on the axial coordinate. Working on the assumption that the interface remains a circular cylinder throughout the motion, we use a numerical method to follow the development of the flow from a specified initial condition and categorise the long-term thread behaviour for different values of the wall amplitude, the viscosity ratio, and the Reynolds number.

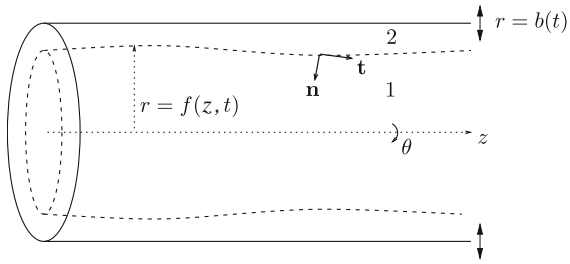

Fig. 1 Illustration of the pulsating pipe flow showing a disturbed interface between the two fluids. The pipe radius, $b(t)$ is a prescribed function of time

2 Flow at zero Reynolds number

We consider the motion of two concentric fluid layers contained within an infinite pipe of circular cross-section whose radius, $b(t)$, is a specified function of time, as is depicted in Fig. 1. The inner fluid, labelled fluid 1, has viscosity μ_1, and the outer fluid, labelled fluid 2, has viscosity μ_2, and both fluids have the same density, ρ. With reference to the cylindrical coordinates (z, r, θ), the wall is located at $r = b(t)$. In the basic, unperturbed flow the interface dividing the layers is a circular cylinder of varying radius located at $r = a(t)$, where $a(t)$ is to be found as part of the solution. The flow is assumed to be axisymmetric and independent of the azimuthal coordinate θ.

The radial and axial velocity components for the unperturbed flow in each fluid, denoted by u_j and w_j respectively for $j = 1, 2$, are given in terms of the unperturbed streamfunctions, ψ_j, by the relations,

$$u_j = -\frac{1}{r}\frac{\partial \psi_j}{\partial z}, \qquad w_j = \frac{1}{r}\frac{\partial \psi_j}{\partial r}.$$

Following [19], we assume a linear dependence on the axial coordinate and write

$$\psi_j = z\, r\, V_j(r, t). \tag{2.1}$$

At zero Reynolds number, the velocity and pressure fields satisfy the equations of Stokes flow,

$$\mathcal{D}^4 \psi_j = 0, \tag{2.2}$$

where the differential operator $\mathcal{D}$ is defined by

$$\mathcal{D}^2 \equiv \frac{\partial^2}{\partial r^2} - \frac{1}{r}\frac{\partial}{\partial r} + \frac{\partial^2}{\partial z^2}. \tag{2.3}$$

Requiring that $u_1 = 0$ and $\partial w_1/\partial r = 0$ at $r = 0$ demands

$$V_1 = 0, \qquad \frac{\partial^2 V_1}{\partial r^2} = 0 \tag{2.4}$$

on $r = 0$, and the no-slip and no-penetration conditions at the pipe wall require

$$V_2 = -\dot{b}, \qquad \frac{\partial V_2}{\partial r} = \frac{\dot{b}}{b}, \tag{2.5}$$

on $r = b(t)$. The velocity and tangential stress fields must be continuous at the interface $r = a(t)$. The dynamic balance of stress at the interface requires that

$$(\boldsymbol{\sigma}_1 - \boldsymbol{\sigma}_2) \cdot \mathbf{n} = 2\gamma\kappa\, \mathbf{n}, \tag{2.6}$$

at $r = a(t)$, where $\boldsymbol{\sigma}_j$ is the Newtonian stress tensor in the jth fluid, γ is the surface tension, $\kappa \equiv (1/2)\nabla\mathbf{n}$ is the mean curvature of the interface, and $\mathbf{n}$ is the unit normal to the interface pointing into the inner fluid. Accordingly, the tangential balance of stress dictates that

$$\left[\mu_j\left(\frac{\partial^2 V_j}{\partial r^2} + \frac{1}{r}\frac{\partial V_j}{\partial r} - \frac{V_j}{r^2}\right)\right]_2^1 = 0, \tag{2.7}$$

where $[\,\cdot\,]_2^1$ denotes the jump in the bracketed quantity across the interface, and the normal balance of stress requires

$$\left[\mu_j\left(\frac{\partial^3 V_j}{\partial r^3}+\frac{2}{r}\frac{\partial^2 V_j}{\partial r^2}-\frac{1}{r^2}\frac{\partial V_j}{\partial r}+\frac{V_j}{r^3}\right)\right]_2^1=0. \tag{2.8}$$

The solution satisfying all the boundary and interfacial conditions is given by

$$\begin{aligned} V_1&=\frac{\dot b}{1+(\lambda-1)s^4}\left[\lambda\left(\frac{r}{b}\right)^3-2(1+(\lambda-1)s^2)\frac{r}{b}\right],\\ V_2&=\frac{\dot b}{1+(\lambda-1)s^4}\left[\left(\frac{r}{b}\right)^3-\frac{2r}{b}-\frac{b}{r}(\lambda-1)s^4\right], \end{aligned} \tag{2.9}$$

where $\lambda=\mu_2/\mu_1$ is the viscosity ratio, and the reduced thread radius

$$s(t)=a(t)/b(t). \tag{2.10}$$

When the viscosities are equal, (2.9) reduces to the Stokes-flow solution given by Blyth et al. [19] for a single fluid. For general values of the viscosity ratio, λ, the kinematic condition at the interface yields an evolution equation for $a(t)$, given by $\mathrm{d}a/\mathrm{d}t=u(r=a)=-V_1(r=a)$. Equivalently,

$$\frac{\mathrm{d}s}{\mathrm{d}t}=\frac{\dot b}{b(1+(\lambda-1)s^4)}\,s\,\left(1+(\lambda-2)s^2-(\lambda-1)s^4\right). \tag{2.11}$$

It is clear from (2.11) that for a pulsatile wall motion, the basic solution (2.9) is synchronous with the wall, as is to be expected in the absence of inertia. In the analogous two-dimensional problem in a channel studied by Blyth [18], there exists an initial value of the layer thickness ratio, for which $\mathrm{d}s/\mathrm{d}t=0$ throughout the motion. In contrast, there is no such value for the axisymmetric problem studied here and the interface always oscillates about a mean value.

3 Linear stability at zero Reynolds number

We examine the stability of the basic flow discussed in the previous section by introducing an axial, spatially periodic disturbance in the interface shape, as shown in Fig. 1. The interface is deflected to the new position given by

$$r(t)=f(z,t)=a(t)+\epsilon\,\eta(z,t), \tag{3.1}$$

where ϵ is a small parameter. To study a spatially periodic deflection, we assume that $\eta=A_1(t)\cos[k(t)z]$, where the wave amplitude, $A_1(t)$, and the wave number, $k(t)$, are both functions of time. Consistent with the form of this perturbation, the streamfunctions in the two fluids are expanded by writing

$$\psi_j=\psi_j^{(0)}(z,r,t)+\epsilon\,\psi_j^{(1)}(z,r,t)+\cdots, \tag{3.2}$$

where the basic flow streamfunctions, $\psi_j^{(0)}(z,r,t)$ are given by (2.1) and (2.9). The velocity and pressure fields are expanded in a similar manner. Following Pozrikidis and Blyth [20], we decompose the disturbance streamfunctions in either fluid into a periodic part and a part which is odd in z by writing

$$\psi_j^{(1)}(z,r,t)=A_1\left(\phi_j(\hat r)\,\sin[k(t)z]+k(t)z\,\chi_j(\hat r)\,\cos[k(t)z]\right), \tag{3.3}$$

where $\hat r=kr$. The second, aperiodic term is included to ensure continuity of the horizontal velocity perturbation at the disturbed interface. We write the corresponding perturbation pressure fields in the form

$$p_j^{(1)}(z,r,t)=A_1\,\mu_j\,\left(q_j(r,t)\,\cos[k(t)z]+k(t)z\,Q_j(r,t)\,\sin[k(t)z]\right), \tag{3.4}$$

for $j=1,2$.

At the origin, $r=0$, the assumption of axisymmetric flow requires

$$u_1^{(1)}=0,\quad \frac{\partial w_1^{(1)}}{\partial r}=0. \tag{3.5}$$

The no-slip and no-penetration conditions at the pipe wall require that

$$\phi_2 = \chi_2 = \frac{\partial \phi_2}{\partial r} = \frac{\partial \chi_2}{\partial r} = 0 \tag{3.6}$$

at $r = b(t)$. The tangential component of the dynamic-stress conditions (2.6) requires

$$\left[2\mu_j \frac{\partial \eta}{\partial z} \left(\frac{\partial w_j^{(0)}}{\partial z} - \frac{\partial u_j^{(0)}}{\partial r} \right) - \mu_j \frac{\partial u_j^{(1)}}{\partial z} - \left\{ \mu_j \left(\frac{\partial w_j^{(1)}}{\partial r} + \eta \frac{\partial^2 w_j^{(0)}}{\partial r^2} \right) \right\} \right]_2^1 = 0, \tag{3.7}$$

where $[\,\cdot\,]_2^1$ denotes the jump in the bracketed quantity across the interface. Substituting in the preceding expressions yields two relations between the unknown coefficients. The normal component of (2.6) requires

$$\left[\left\{ -\eta \frac{\partial p_j^{(0)}}{\partial r} - p_j^{(1)} \right\} + 2\mu_j \, \eta \frac{\partial^2 u_j^{(0)}}{\partial r^2} + 2\mu_j \frac{\partial u_j^{(1)}}{\partial r} \right]_2^1 = \gamma \left(\frac{\eta}{a^2} + \frac{\partial^2 \eta}{\partial z^2} \right), \tag{3.8}$$

with all terms evaluated at the unperturbed interface $r = a(t)$. Continuity of the horizontal and radial velocities at the interface demands

$$u_1^{(1)} + \eta \frac{\partial u_1^{(0)}}{\partial r} = u_2^{(1)} + \eta \frac{\partial u_2^{(0)}}{\partial r}, \qquad w_1^{(1)} + \eta \frac{\partial w_1^{(0)}}{\partial r} = w_2^{(1)} + \eta \frac{\partial w_2^{(0)}}{\partial r}, \tag{3.9}$$

where all terms are evaluated at $r = a(t)$.

The kinematic condition at the interface requires that

$$\frac{\partial \eta}{\partial t} + w_1^{(0)} \frac{\partial \eta}{\partial z} - \eta \frac{\partial u_1^{(0)}}{\partial r} - u_1^{(1)} = 0, \tag{3.10}$$

with all terms evaluated at $r = a(t)$. Substituting the previous results, we derive the evolution equation for the wave number,

$$\frac{\mathrm{d}k}{\mathrm{d}t} + \left(\frac{\partial V_1}{\partial r} + \frac{V_1}{r} \right) k + \frac{\chi_1}{r} \, k^2 = 0, \tag{3.11}$$

where all terms are evaluated at $r = a(t)$, and the evolution equation for the interfacial perturbation amplitude,

$$\frac{\mathrm{d}A_1}{\mathrm{d}t} + \mathcal{L}(t) A_1 = 0, \tag{3.12}$$

with

$$\mathcal{L}(t) = \frac{\partial V_1}{\partial r} + \frac{k}{a} \phi_1 + \frac{k}{a} \chi_1, \tag{3.13}$$

where each term is evaluated at $r = a(t)$. All of the terms in (3.11) are independent of A_1; hence the evolution equation for k is decoupled from the evolution equation for A_1.

In the next subsection, we consider the particular details of the stability analysis for disturbances of large wavelength. Subsequently, we consider the evolution of a disturbance of arbitrary wavelength under the general conditions of Stokes flow.

3.1 Longwave analysis

Working on the assumption that variations in the z-direction are small compared to variations in the radial direction, the Stokes momentum equations reduce to the lubrication equations in either fluid, $j = 1, 2$,

$$0 = -\frac{\mathrm{d}p_j}{\mathrm{d}z} + \mu_j \frac{1}{r} \frac{\partial}{\partial r} \left(r \frac{\partial w_j}{\partial r} \right), \tag{3.14}$$

$$0 = \frac{\partial u_j}{\partial r} + \frac{u_j}{r} + \frac{\partial w_j}{\partial z}, \tag{3.15}$$

where the pressure does not vary in the radial direction. For the basic flow, when the interface between the two fluids remains a circular cylinder throughout the motion, the stream functions for the basic flow are given by (2.9), and the basic pressure field in fluid 1 is given by

$$p_1^{(0)} = \frac{8\mu_1\lambda\dot{b}}{b^3(1+(\lambda-1)s^4)}\,z^2 + \frac{\gamma}{a}, \qquad p_2^{(0)} = p_1^{(0)} + \frac{\gamma}{a^2}\eta. \tag{3.16}$$

By substituting the expansions (3.2) in the reduced equations (3.14), we obtain at first order

$$\tilde{\mathcal{D}}^4\psi_j^{(1)} = 0, \tag{3.17}$$

where $\tilde{\mathcal{D}}^2 \equiv \partial^2/\partial r^2 - (1/r)\partial/\partial r$. Substituting (3.3) in (3.17) and solving, we obtain

$$\begin{aligned}\phi_j &= \tilde{a}_{1j}(t) + \tilde{a}_{2j}(t)\hat{r}^2 + \tilde{a}_{3j}\hat{r}^2\log\hat{r} + \tilde{a}_{4j}(t)\hat{r}^4,\\ \chi_j &= \tilde{b}_{1j}(t) + \tilde{b}_{2j}(t)\hat{r}^2 + \tilde{b}_{3j}\hat{r}^2\log\hat{r} + \tilde{b}_{4j}(t)\hat{r}^4,\end{aligned} \tag{3.18}$$

for $j = 1, 2$, where $\hat{r} = kr$. The conditions of axisymmetry at the origin (3.5) demand that $\tilde{a}_{11} = \tilde{a}_{31} = \tilde{b}_{11} = \tilde{b}_{31} = 0$. For the dynamic stress balance at the interface, $r = a(t)$, under the present longwave assumption only the terms in curly brackets on the left-hand sides of the tangential stress condition (3.7) and the normal-stress condition (3.8) need be retained. Overall, the boundary conditions (3.5)–(3.9) contribute 16 conditions for the 16 unknowns, which we assemble into the matrix system

$$\mathbf{M}(\mathrm{t})\mathbf{w} = \mathbf{c}(\mathrm{t}), \tag{3.19}$$

where $\mathbf{M}$ is a known 16×16 matrix, the solution vector $\mathbf{w} = (\tilde{a}_{11}, \ldots, \tilde{b}_{42})^T$ and $\mathbf{c}$ is the vector of inhomogeneous terms. Note that (3.19) is independent of A_1.

We consider the case when the wall position, $b(t)$, is a periodic function of time, and take

$$b(t) = b^*(1 + \Delta\sin nt), \tag{3.20}$$

where b^*, n, and Δ are real constants, with $0 < \Delta < 1$. With this assumption, the basic flow (2.9) is periodic in time with period $T = 2\pi/n$. Floquet theory dictates that a small perturbation from a time-periodic solution may be expressed as the product of an exponentially growing part and a time-periodic part (e.g. [21, Chap. 5.4]). Noting the form of (3.3), we therefore write

$$A_1 = e^{\sigma t}A(t), \tag{3.21}$$

where σ is the Floquet exponent and $A(t)$ is a periodic function of time such that $A(t + T) = A(t)$. As a consequence, the coefficients $\tilde{a}_{ij}$, $\tilde{b}_{ij}$, for $i = 1, \ldots, 4$ and $j = 1, 2$, are all periodic with period T. From the linear system (3.19), the wave number $k(t)$ must also be periodic with period T. The stability of the system is determined by calculating the Floquet exponent σ: if $\sigma > 0$ the flow is unstable, and if $\sigma < 0$ the flow is stable.

Since the wavenumber of a disturbance varies periodically in time according to (3.11), it is sufficient to consider the stability of the system to perturbations over a range of wavenumbers, each introduced into the flow at $t = 0$. Introducing a particular disturbance later into the wall pulsation cycle simply corresponds to introducing a disturbance of a slightly different wavelength at $t = 0$. To compute the Floquet exponent, we integrate (3.12) over one time period to obtain

$$\sigma = \frac{1}{T}\log\left\{\frac{A_1(T)}{A_1(0)}\right\} = -\frac{1}{T}\int_0^T \mathcal{L}(t)\,\mathrm{d}t. \tag{3.22}$$

It follows that, since $\mathcal{L}(t)$ is periodic with period T, the Floquet exponent does not depend on the pulsation frequency n. Consequently, the stability of the system depends upon the amplitude of the pulsations, Δ, the viscosity ratio λ, and the initial dimensionless thread radius,

$$\delta = s(0) = a(0)/b^*. \tag{3.23}$$

Since the velocity components of the basic flow are periodic with zero mean, the first term in (3.13) makes no contribution to the growth rate (3.22). Moreover, dividing (3.11) by $k(t)$ and integrating over one time period, we see that the third term in (3.13) also does not contribute to the growth rate, so that

$$\sigma = -\frac{1}{T}\int_0^T \frac{k}{a}\phi_1(a)\,\mathrm{d}t. \tag{3.24}$$

Integrating (3.11), we find

$$k = \frac{cs^4}{1+(\lambda-1)s^4}, \tag{3.25}$$

where c is a constant of integration determined by the choice of the initial wavenumber $k_0 = k(0)$ and thread radius δ. The form (3.25) confirms that the wavenumber is periodic with period T.

Solving the linear system (3.19), we find that

$$\frac{k}{a}\phi_1(a) = \frac{c^2\gamma_0}{16\mu_1\lambda}\,\frac{bs^9}{(1+(\lambda-1)s^4)^3}\left[4(1+(\lambda-1)s^4)\log s + (4-3\lambda)s^4 + 4(\lambda-2)s^2 + 4 - \lambda\right]. \tag{3.26}$$

Integrating (2.11) and rearranging, we can obtain the explicit form of $s(t)$ in terms of the known wall function $b(t)$. In the simplest case of equal viscosity fluids, we have

$$s = \frac{b}{(b^2+\alpha^2)^{1/2}}, \tag{3.27}$$

where $\alpha^2 = [b(0)/a(0)]^2[b^2(0) - a^2(0)]$. Substituting (3.26) in (3.24), we compute the longwave growth rate which takes the form

$$\sigma = \left(\frac{\gamma}{\mu_1 b^*}\right)\tau(\delta;\lambda;\Delta)\,(k_0 b^*)^2, \tag{3.28}$$

where τ depends on the dimensionless initial thread radius, δ, the viscosity ratio, λ, and the amplitude of the wall pulsations, Δ. The growth rate is computed by evaluating the integral in (3.24) using the trapezium rule.

For equal viscosity fluids, $\lambda = 1$, when $\delta = 0.5$ we find that τ increases as Δ increases and the pulsations exacerbate the instability. In particular, $\tau = 0.02219$ for $\Delta = 0$, $\tau = 0.02318$ for $\Delta = 0.1$ and $\tau = 0.02605$ for $\Delta = 0.2$. In Fig. 2, we see how the stability coefficient, τ, has quite different behaviour for different values of the viscosity ratio and different values of the initial thread radius. When $\delta = 0.5$, as shown in Fig. 2a, the pulsations increase the growth rate of longwave disturbances provided the viscosity ratio is sufficiently small. For a large value of λ, corresponding to a very viscous annular layer, the pulsations reduce the growth rate and have a stabilising influence on the flow. The situation is markedly different for larger values of δ and thinner annular films. The sample case $\delta = 0.8$ shown in Fig. 2b shows that for low values of the viscosity ratio, the pulsations decrease the growth rate. When λ is sufficiently large, the dependence of τ on Δ is non-monotonic and the pulsations first increase and then decrease the growth rate of longwave disturbances.

With respect to the application of the analysis to the human lung, where longwave disturbances are expected ([3, 22]), measurements for the airway diameter and the thickness of the interior liquid lining suggest $\delta \approx 0.96$ ([2]). Taking the limit $\lambda \to \infty$ in the present analysis, we effectively obtain an annular fluid layer surrounding a gas at constant pressure. The basic flow in the annular layer is purely radial, given by $u_2 = b\dot{b}/r$ and there is no flow in the axial direction. Taking $\delta = 0.96$, we find that the growth rate of longwave linear disturbances increases as the amplitude of the pulsations increases. Beyond a certain value of Δ which lies below 1, the present model predicts negative values of $a(t)$ during one time period, which is physically inadmissible.

3.2 Stokes-flow analysis

Relaxing the assumption of longwave disturbances, we substitute the expansions (3.2) in the Stokes equations, eliminate the pressure, and derive at first order the governing equations for the perturbation streamfunctions in fluid $j = 1, 2$,

$$\mathcal{D}^4\psi_j^{(1)} = 0. \tag{3.29}$$

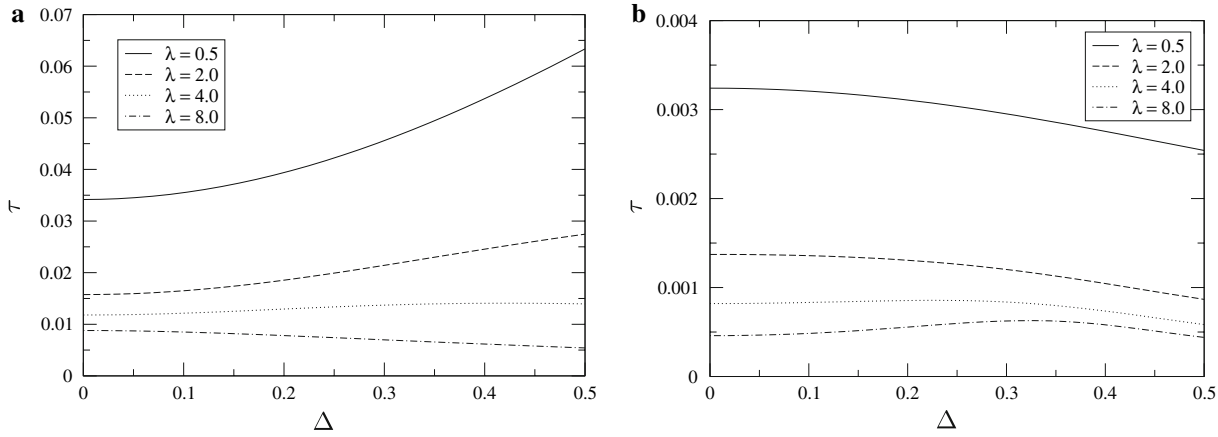

Fig. 2 The longwave stability coefficient τ for **a** $\delta = 0.5$ and **b** $\delta = 0.8$ plotted against the pulsation amplitude, Δ, for various values of the viscosity ratio, λ

Substituting (3.3) in (3.29) and solving, we obtain

$$\phi_j = a_{1j}(t)krI_1(kr) + a_{2j}(t)krK_1(kr) + 4k^2r\,\Phi_j,$$
$$\chi_j = b_{1j}(t)krI_1(kr) + b_{2j}(t)krK_1(kr) + \alpha_j(t)krU_1(r) + \beta_j(t)krU_2(r), \tag{3.30}$$

for $j = 1, 2$, where

$$\Phi_j = I_1(kr)\int R_j(r)\,K_1(kr)\,\mathrm{d}r - K_1(kr)\int R_j(r)\,I_1(kr)\,\mathrm{d}r, \tag{3.31}$$
$$R_j = c_{1j}(t)krI_1(kr) + c_{2j}(t)krK_1(kr) + \alpha_j(t)krU_1(r) + \beta_j(t)krU_2(r), \tag{3.32}$$

with

$$U_1 = I_1(kr)\int krI_1(kr)K_1(kr)\,\mathrm{d}r - K_1(kr)\int krI_1^2(kr)\,\mathrm{d}r, \tag{3.33}$$
$$U_2 = I_1(kr)\int krK_1^2(kr)\,\mathrm{d}r - K_1(kr)\int krI_1(kr)K_1(kr)\,\mathrm{d}r. \tag{3.34}$$

The 16 functions $a_{ij}, b_{ij}, c_{ij}, \alpha_j, \beta_j, i = 1, 2, j = 1, 2$ are to be determined. The constants of integration associated with the indefinite integrals in (3.31)–(3.34) are taken to be zero without loss of generality. We note that the second and first integrals in (3.33) and (3.34) respectively can be performed exactly (e.g. [23, Chap. 11]). Moreover, by expanding for small kr and retaining the leading-order contributions, it can be shown that (3.30) reduces to the longwave form (3.18).

By substituting (3.4) in the horizontal component of the Stokes momentum equation, we find

$$q_j = -\frac{1}{kr}\frac{\mathrm{d}}{\mathrm{d}r}\left[\frac{\mathrm{d}^2\phi_j}{\mathrm{d}r^2} - \frac{1}{r}\frac{\mathrm{d}\phi_j}{\mathrm{d}r}\right] + \frac{k}{r}\frac{\mathrm{d}\phi_j}{\mathrm{d}r} + 2\frac{k}{r}\frac{\mathrm{d}\chi_j}{\mathrm{d}r} + Q_j,$$
$$Q_j = \frac{1}{kr}\frac{\mathrm{d}}{\mathrm{d}r}\left[\frac{\mathrm{d}^2\chi_j}{\mathrm{d}r^2} - \frac{1}{r}\frac{\mathrm{d}\chi_j}{\mathrm{d}r}\right] - \frac{k}{r}\frac{\mathrm{d}\chi_j}{\mathrm{d}r}. \tag{3.35}$$

The boundary conditions (3.5)–(3.9) provide 16 linear equations for the 16 unknown functions which can be assembled into a matrix system similar to (3.19) which is independent of the perturbation amplitude, A_1. Assuming that A_1 adopts the form given in (3.21), to determine the stability of the system to a disturbance of chosen initial wavenumber, we integrate (3.11) and (3.12) forward in time numerically using second-order Runge–Kutta integration from $t = 0$ up to $t = T$. At each part of the integration step, the 16×16 linear system is solved to find the unknown T-periodic functions $a_{ij}(t)$, $b_{ij}(t)$, $c_{ij}(t)$, $\alpha_j(t)$, $\beta_j(t)$ at the present time level. The growth rate is given

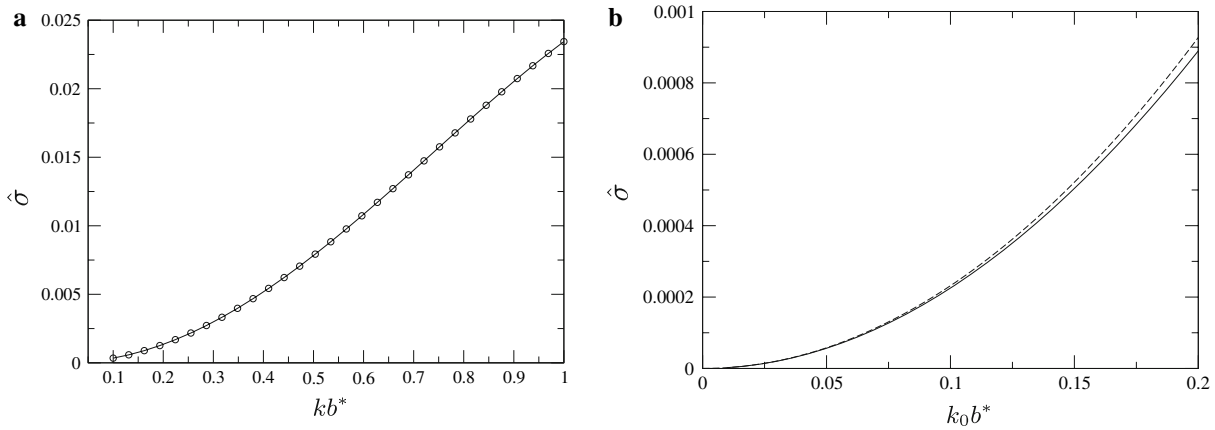

Fig. 3 **a** Dimensionless growth $\hat{\sigma}$ versus dimensionless wave number kb^* when $\lambda = 0.5$, $\delta = 0.5$ for a pipe of fixed radius, $\Delta = 0$. The solid lines are the current results; the results of Kwak and Pozrikidis [11] are shown as circles. **b** Comparison of the longwave prediction $0.02318(k_0 b^*)^2$, shown with a broken line, and the growth rate for Stokes flow, shown with a solid line, for the case $\lambda = 1$, $\delta = 0.5$, and $\Delta = 0.1$; the growth rates are plotted against the dimensionless initial wavenumber $k_0 b^*$

by evaluating the formula (3.22) numerically. As in Sect. 3.1, the growth rate depends upon the amplitude of the pulsations, Δ, the viscosity ratio λ, and the initial dimensionless thread radius δ defined in (3.23).

To check the numerical computations, we consider the stability of quiescent fluids in a pipe of fixed radius, so that $\Delta = 0$. Goren [9] studied the case of a viscous layer coating the inside of a cylindrical tube, which corresponds to the limit $\lambda \to \infty$ in the present formulation. We have confirmed that our computed growth rates reduce to those computed by Goren in this limit. Kwak and Pozrikidis [11] carried out an analysis for a liquid thread surrounded by an annular layer inside a cylindrical tube in the presence of an insoluble surfactant. In Fig. 3a, we display the dimensionless growth rate $\hat{\sigma} \equiv (\mu_1 b^*/\gamma)\sigma$ for the case $\lambda = 0.5$, when $\delta = 0.5$, over a range of dimensionless wave numbers kb^*. The solid line shows the results of the present calculation. The circles are the predictions of Kwak and Pozrikidis for a clean interface free of surfactant. The agreement between the two sets of results is excellent. In Fig. 3b, the longwave prediction for $\Delta = 0.1$ is shown to agree very well with the present growth rate for Stokes flow. When there are no pulsations, the longwave prediction almost coincides with results for Stokes flow over the same range of wavenumbers as are shown in Fig. 2a. As Δ increases, the agreement between the longwave and Stokes-flow predictions occurs over a shorter range of wavelengths.

In Fig. 4a, b we show the effect of wall pulsations on the growth rate over a range of dimensionless initial wavenumbers, $k_0 b^*$, for a number of values of Δ for the two different initial thread radii $\delta = 0.5$ and $\delta = 0.25$ when $\lambda = 0.5$ and the annular layer is less viscous than the thread. In all cases, the growth rate is negative above a critical cut-off value $(k_0 b^*)_{\text{crit}}$ and the flow is stable. In the absence of pulsations, $\Delta = 0$, the growth rate traced by the thin solid line passes through zero at $k_0 b^* = 2$ in accordance with the critical Rayleigh instability threshold. As predicted by the longwave theory, the effect of the pulsations at small wavenumbers is to increase the growth rate. The increase is imperceptible in Fig. 4a for $\delta = 0.5$, but is clearly visible in Fig. 4b for $\delta = 0.25$. For larger wavenumbers, the growth rate goes down as Δ increases. In Fig. 4a, b, the maximum growth rate over all wavenumbers decreases as Δ is increased from zero, and in this sense the pulsations have a stabilising effect on the flow. The same observation holds when $\lambda = 2.0$, so that the annular layer is more viscous than the thread, and the other parameter values used to produce these figures are kept the same.

The longwave analysis suggests that, when δ is near unity and the annular layer is thin, the pulsations tend to lower the growth rate of small wavenumber disturbances. This can be seen in Fig. 5a for the case $\delta = 0.9$. Consistent with the longwave theory, as Δ is increased from zero, the wall vibrations reduce the growth rate of small wavenumber disturbances and delay the disintegration of the annular film into isolated lobes. The maximum growth rates over all wavenumbers in Fig. 5a is achieved when $\Delta = 0$ and there is no wall motion. In other words, the pulsations decrease the growth rate of the most unstable wave. However, when $\lambda = 2.0$ and the annular layer is

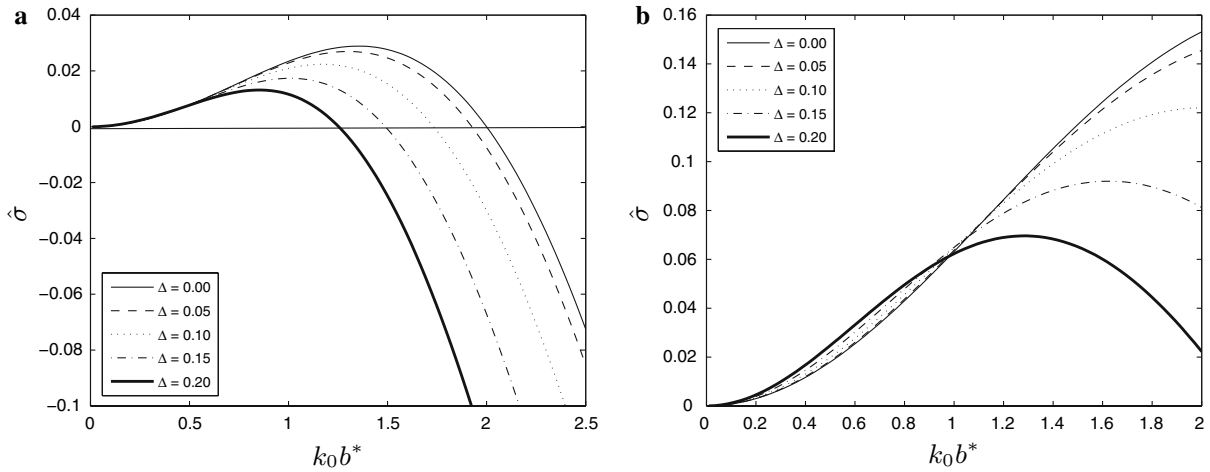

Fig. 4 Growth rate $\hat{\sigma}$ versus reduced initial wave number $k_0 b^*$ for $\lambda = 0.5$ and various wall amplitudes Δ when **a** $\delta = 0.5$, **b** $\delta = 0.25$

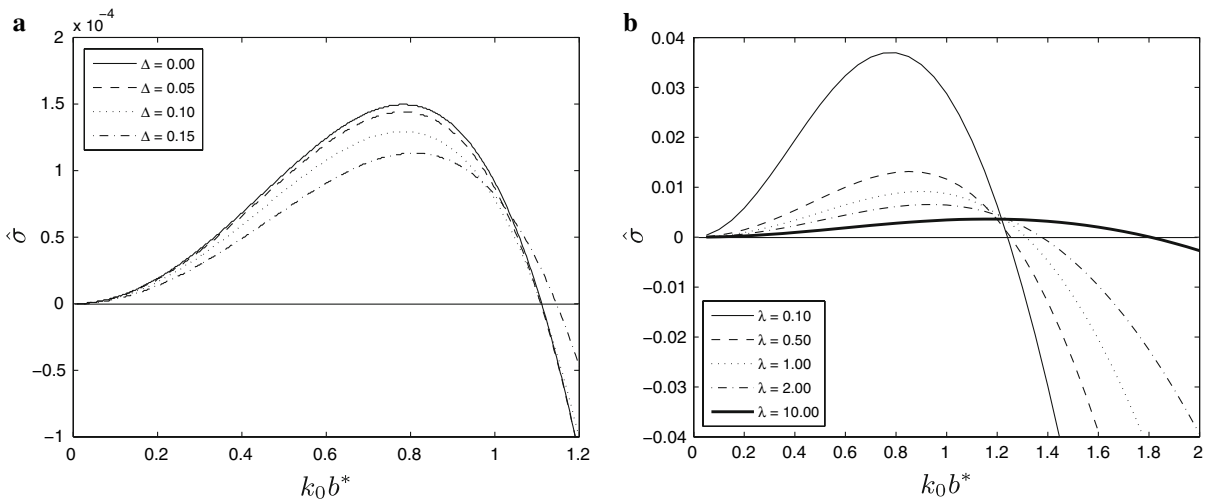

Fig. 5 **a** Growth rate $\hat{\sigma}$ versus reduced initial wave number $k_0 b^*$ for $\lambda = 0.5$ and various wall amplitudes Δ when $\delta = 0.9$. **b** Growth rate $\hat{\sigma}$ versus $k_0 b^*$ for $\delta = 0.5$, $\Delta = 0.2$ and various values of λ

more viscous than the thread (with the other parameter values kept the same as in Fig. 5a), the growth rate decreases as the pulsation amplitude is raised.

Figure 5b illustrates the effect of varying the viscosity ratio on the growth rates for the sample case $\delta = 0.5$ and $\Delta = 0.2$. The viscosity ratio has a significant effect on the maximum growth rate, which decreases as λ increases and the annular layer becomes increasingly more viscous than the thread. The same qualitative features are found for a thin annular film with $\delta = 0.9$. With no pulsations, $\Delta = 0$, the cut-off wavenumber is equal to the Rayleigh threshold value $k_0 b^* \delta$, which is independent of λ. For the moderate initial thread radius $\delta = 0.5$, the cut-off wavenumber decreases monotonically as Δ increases for any fixed value of λ. For thin annular layers, however, the behaviour is non-monotonic, as can be seen in Fig. 6a. Note that in this figure the cut-off wavenumber approaches the Rayleigh threshold $k_0 b^* \delta = 1.111$ as Δ approaches zero. When Δ is fixed, the cut-off wavenumber varies non-monotonically as λ increases, as is demonstrated in Fig. 6a for the case $\delta = 0.5$ and $\Delta = 0.2$. For any value of the viscosity ratio, λ, and for the moderate thread radius $\delta = 0.5$, increasing λ reduces the size of the maximum growth rate over all wavenumbers. For a thin annular film with $\delta = 0.9$ and $\lambda = 0.5$, on increasing Δ the maximum growth rate decreases to a minimum value and then starts to increase.

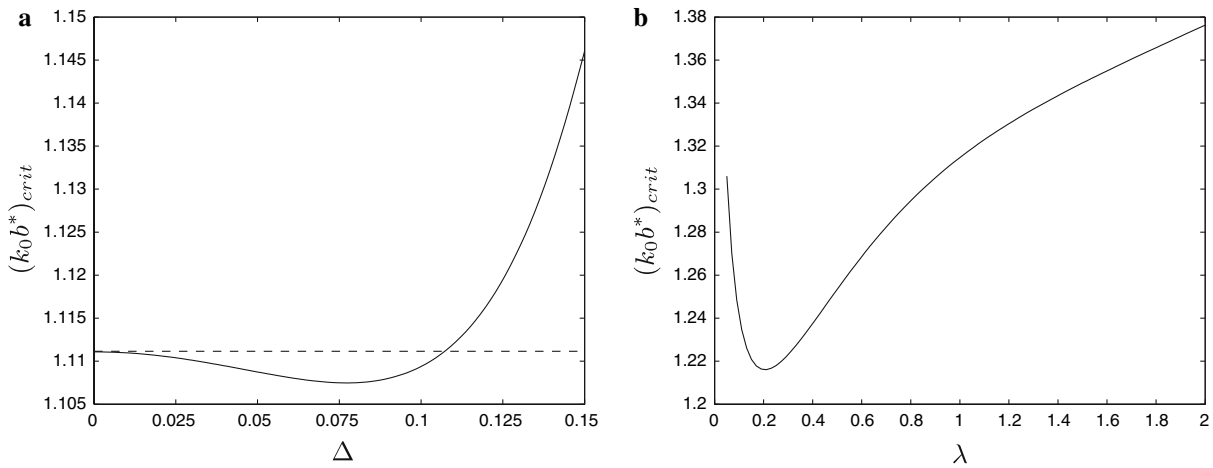

Fig. 6 **a** The critical cut-off wave number $(k_0 b^*)_{\text{crit}}$ against Δ for $\lambda = 0.5$ when $\delta = 0.9$; the broken line indicates the Rayleigh threshold $k_0 b^* \delta = 1.111$. **b** The cut-off wave number, $(k_0 b^*)_{\text{crit}}$, against λ for $\delta = 0.5$ and $\Delta = 0.2$

4 Flow at arbitrary Reynolds number

We now turn to the case of pulsating flow at finite Reynolds number. Our goal in this section is to extend the basic flow solution discussed in Sect. 2 for Stokes flow to include inertia. We assume that the interface is a circular cylinder of variable radius throughout the motion. The fluids are assumed to have equal density but have generally different viscosities. We consider only a periodic pulsating motion, with the pipe radius given by $b(t) = b_0(1 + \Delta \cos nt)$. This is slightly different to the form (3.20) adopted in Sect. 3, and is chosen so that the wall velocity is zero at $t = 0$ for numerical convenience. We seek a similarity solution in which both the axial velocity and vorticity have a linear dependence on the axial coordinate, z. To this end, we write

$$\psi_j = z\, r V_j(r,t), \qquad \omega_j = -\nabla^2 \psi_j = z\, G_j(r,t), \tag{4.1}$$

for $j = 1, 2$, where ω_j is the sole vorticity component in the azimuthal direction, and the functions V_j and G_j are to be found.

We nondimensionalize variables using $1/n$ as the time scale and the mean pipe radius b_0 as the length scale, and write $t = nt^*$, $(z, r) = b_0(z^*, r^*)$, $\psi_j = (nb_0^3)\,\psi_j^*$, and $\omega = n\omega^*$, where asterisks indicate dimensionless variables. For numerical convenience, it is advantageous to map the flow region onto a domain in which the pipe wall is fixed. To achieve this we introduce the new coordinate $\eta = r/b(t)$, so that the fluid occupies the region $0 \le \eta \le 1$. Discarding the asterisk superscripts, the Navier–Stokes equations in each fluid reduce without approximation to the form,

$$\frac{\partial G_j}{\partial t} - \frac{\dot b}{b}\eta \frac{\partial G_j}{\partial \eta} + \frac{1}{b}\left(G_j \frac{\partial V_j}{\partial \eta} - V_j \frac{\partial G_j}{\partial \eta}\right) + \frac{2V_j G_j}{b\eta} = \frac{\lambda_j}{b^2 R}\left(\frac{\partial^2 G_j}{\partial \eta^2} + \frac{1}{\eta}\frac{\partial G_j}{\partial \eta} - \frac{G_j}{\eta^2}\right), \tag{4.2}$$

$$G_j = -\frac{1}{b^2}\left(\frac{\partial^2 V_j}{\partial \eta^2} + \frac{1}{\eta}\frac{\partial V_j}{\partial \eta} - \frac{V_j}{\eta^2}\right), \tag{4.3}$$

where $j = 1, 2$, $\lambda_1 = 1$ and $\lambda_2 = \lambda = \mu_2/\mu_1$, and the Reynolds number $R = \rho n b_0^2/\mu_1$. The no-slip and no normal flow conditions at the wall require

$$V_2(1,t) = -\dot b, \qquad \frac{\partial V_2}{\partial \eta}(1,t) = \dot b. \tag{4.4a, b}$$

At the origin, $r = 0$, we demand that

$$V_1(0,t) = 0, \qquad G_1(0,t) = 0, \tag{4.5a, b}$$

in order that both u_1 and $\partial w_1/\partial\eta$ are zero on the pipe axis in accordance with axisymmetric flow. At the interface, $\eta = s(t)$, where the reduced thread radius $s(t) = a(t)/b(t)$, continuity of velocity requires

$$V_1 = V_2, \qquad \frac{\partial V_1}{\partial \eta} = \frac{\partial V_2}{\partial \eta}, \tag{4.6a, b}$$

and continuity of the tangential stress requires

$$G_1 = \lambda G_2. \tag{4.7}$$

The kinematic condition at the interface yields an evolution equation for the interfacial radius, $a(t)$,

$$\frac{\mathrm{d}a}{\mathrm{d}t} = -V_1(s, t). \tag{4.8}$$

One further condition is found by integrating (4.2) across the moving interface from $\eta = s^-(t)$ up to $\eta = s^+(t)$ and using (4.8) to obtain

$$\frac{\partial G_1}{\partial \eta} = \lambda \frac{\partial G_2}{\partial \eta}. \tag{4.9}$$

The solution to the problem at zero Reynolds number, $R = 0$, was given in (2.9). When inertia is present, $R \neq 0$, it is necessary to compute the solution numerically.

4.1 Numerical method

Although we are working in a domain where the pipe wall is fixed, the interfacial position is still time-dependent. To remedy this awkward situation, we change coordinates and introduce the time-dependent piecewise linear mapping

$$\zeta = \frac{\eta - s}{s} \quad \text{for} \quad \eta \leq s, \qquad \zeta = \frac{\eta - s}{1 - s} \quad \text{for} \quad \eta \geq s. \tag{4.10}$$

This single-valued transformation maps $\eta \in [0, 1]$ to the new variable $\zeta \in [-1, 1]$. In the new coordinate system the interface is located at $\zeta = 0$, the wall is located at $\zeta = 1$, and the pipe axis is located at $\zeta = -1$. To integrate the system (4.2)–(4.9) forward in time, we use a modified version of the numerical method described by Blyth [18] for channel flow which is suited to the present stream-function–vorticity formulation. Essentially, given knowledge of the stream-function V_j and vorticity G_j at the current time, we integrate (4.2) forward one time step using the Crank–Nicolson method. Next, we update the vorticity by solving (4.3), and the procedure is repeated.

We use a spatial grid with mesh points at $\zeta_i = -1 + (i - 1)\delta\zeta$, for $i = 1, \ldots, 2N + 1$, where $\delta\zeta = 1/N$ is the uniform grid spacing. Our aim is to obtain the solution over the grid at the general time level $t = t_n = n\delta t$, where δt is the time step. We label the stream function and vorticity in either fluid at the grid point ζ_i and the time level t_n as $G^n_{j,i}$ and $V^n_{j,i}$ for $j = 1, 2$. Equations (4.2) and (4.3) are discretized using central differences in space. In order to maintain second-order accuracy, we centre the linear terms at the midpoint between time levels, that is $t_n + \frac{1}{2}\delta t$, in the usual way for Crank–Nicolson integration. At the preliminary stage, the nonlinear terms are treated explicitly at the current time t_n.

The boundary conditions (4.4a, b), (4.5a, b), (4.6a, b) and (4.7) yield the grid values,

$$\begin{aligned} &V^n_{2,2N+1} = -\dot{b}(t_n), \qquad V^n_{1,1} = 0, \qquad G^n_{1,1} = 0, \\ &V^n_{1,N+1} = V^n_{2,2N+1}, \qquad G^n_{1,N+1} = \lambda G^n_{2,2N+1}. \end{aligned} \tag{4.11}$$

Introducing the fictitious point $V^n_{2,2N+2}$ in fluid 2, we derive the condition

$$\frac{V^n_{2,2N+2} - V^n_{2,2N}}{2\delta\zeta} = [1 - s(t_n)]\, \dot{b}(t_n) \tag{4.12}$$

on discretizing (4.4a, b) using centred differences at the wall $\zeta = \zeta_{2N+1}$.

Next, we apply the discretized forms of (4.2) and (4.3) in each fluid at the interior points, $i = 2, \ldots, N$, and combine these with the boundary equations (4.11) and (4.12). Making guesses for the three unknown values

$$G^{n+1}_{1,N+1}, \qquad V^{n+1}_{1,N+1}, \qquad G^{n+1}_{2,2N+1},$$

we form the matrix systems

$$\mathbf{A} \cdot \mathbf{G}^{n+1} = \mathbf{L}(\mathbf{G}^n) + \mathbf{N}(\mathbf{G}^n, \mathbf{V}^n), \tag{4.13}$$

$$\mathbf{B} \cdot \mathbf{V}^{n+1} = \mathbf{S}(\mathbf{G}^{n+1}), \tag{4.14}$$

where $\mathbf{L}(\mathbf{G}^n)$ and $\mathbf{N}(\mathbf{G}^n, \mathbf{V}^n)$ incorporate the discretized form of the linear and nonlinear terms respectively, which are both evaluated at $t = t_n$, the unknown vectors $\mathbf{V}^n = (V^n_{1,2}, \ldots, V^n_{1,N}, V^n_{2,N+2}, \ldots, V^n_{1,2N})$ and $\mathbf{G}^n = (G^n_{1,2}, \ldots, G^n_{1,N}, G^n_{2,N+2}, \ldots, G^n_{2,2N})$, which exclude the interfacial values $V^n_{1,N+1}$ and $G^n_{1,N+1}$. Both $\mathbf{A}$ and $\mathbf{B}$ are $(2N-2) \times (2N-2)$ tridiagonal matrices. The method proceeds through the following steps.

Step 1: We solve the matrix systems (4.13) and (4.14) using the Thomas algorithm (e.g. [24, Chap. 3.5]). Since $\mathbf{A}$ and $\mathbf{B}$ both require the knowledge of the updated interface position $r(t_{n+1})$, we solve (4.13) and (4.14) simultaneously with the discretized form of the evolution equation (4.8),

$$a(t_{n+1}) = a(t_n) - \frac{1}{2}\delta t\,(V^{n+1}_{1,N+1} + V^n_{1,N+1}), \tag{4.15}$$

noting that $a(t_n) = s(t_n)b(t_n)$.

Step 2: To preserve the second order spatial and temporal accuracy of the method, we employ an iteration scheme similar to that described by Hall and Papageorgiou [25] and Blyth [18]. Denoting the values of $\mathbf{G}^{n+1}$ and $\mathbf{V}^{n+1}$ just computed as $\mathbb{G}$ and $\mathbb{V}$, we centre the nonlinear terms in (4.13) at the mid-point $t_n + \frac{1}{2}\delta t$, by writing

$$\mathbf{A} \cdot \mathbf{G}^{n+1} = \mathbf{L}(\mathbf{G}^n) + \frac{1}{2}\mathbf{N}(\mathbf{G}^n, \mathbf{V}^n) + \frac{1}{2}\mathbf{N}(\mathbb{G}, \mathbb{V}). \tag{4.16}$$

Solving (4.16) in conjunction with (4.14) and (4.15), we obtain updated values of $\mathbf{G}^{n+1}$ and $\mathbf{V}^{n+1}$. Step 2 is repeated until the updated values have converged to within an acceptable tolerance.

Step 3: To refine the three initial guesses of $G^{n+1}_{1,N+1}$, $V^{n+1}_{1,N+1}$ and $G^{n+1}_{2,2N+1}$, we use Newton's method to satisfy the following three objective equations:

(*i*) the discretized form of (4.6a, b) at the interface;
(*ii*) the discretized form of (4.3) at the wall;
(*iii*) the discretized form of (4.9) at the interface.

In (*iii*) we first substitute (4.3) in (4.9) and then introduce the extra fictitious values $V^{n+1}_{1,N+2}$ and $V^{n+1}_{2,N}$. Equations for these values are obtained by applying (4.3) at the interface. Steps 1 to 2 are repeated iteratively until the values of $G^{n+1}_{1,N+1}$, $V^{n+1}_{1,N+1}$ and $G^{n+1}_{2,2N+1}$ have converged to within a prescribed tolerance, whereupon we obtain the final values of $\mathbf{G}^{n+1}$ and $\mathbf{V}^{n+1}$ at the new time level.

To verify the accuracy of the numerical method, we perform a number of checks. First we compare our numerically computed solution for a small value of the Reynolds number with the Stokes-flow solution described in Sect. 2. In Fig. 7a, we show how $s(t)$ varies with time, t, when $R = 0.002$, $\lambda = 0.25$ and $\Delta = 0.2$. The solid line corresponds to the present numerical calculation and the circles correspond to the Stokes solution. The agreement between the two is excellent. Secondly, we compare our results for fluids of equal viscosities, $\lambda = 1$, with the solution for a single fluid given in Blyth et al. [19], when $R = 20$ and $\Delta = 0.2$. In Fig. 7b, we plot the wall vorticity, $G(1, t)$, against time, t, where the solid line corresponds to the current calculation and the circles correspond to the results of Blyth et al. [19]. Again, the agreement between the two sets of results is excellent. As a third check, we compare the trace of $s(t)$ against time for the two different spatial discretization levels and time steps $(N, \delta t) = (100,\ 0.001)$ and $(N, \delta t) = (500,\ 0.0001)$. The two sets of results are almost coincident.

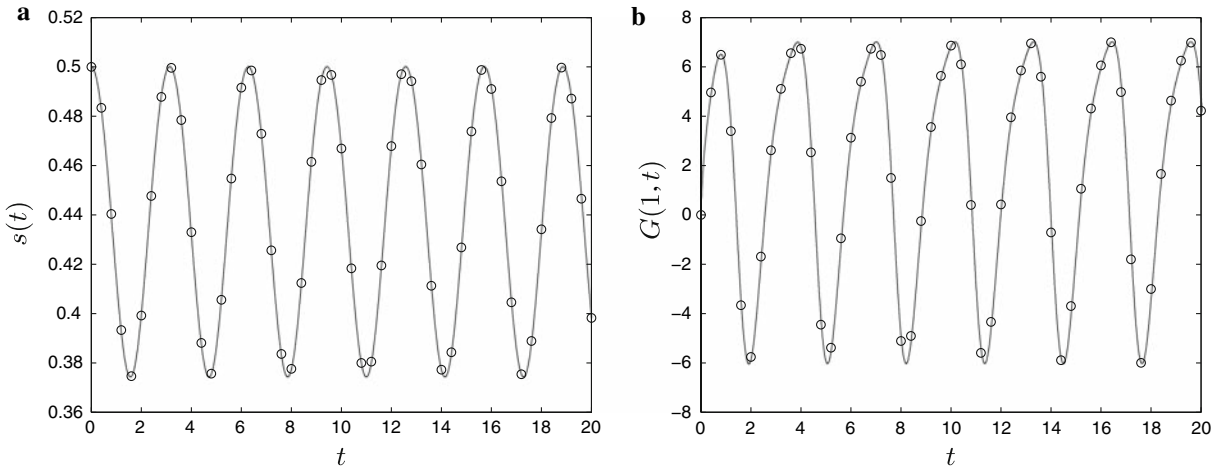

Fig. 7 **a** The reduced thread radius $s(t)$ for the case $\lambda = 0.25$ and $\Delta = 0.2$. The *solid line* shows the numerical solution when $R = 0.002$ and the *circles* show the Stokes solution at $R = 0$. **b** The wall vorticity, $G(1, t)$, for the case $\lambda = 1$, $\Delta = 0.2$ and $R = 20$. The *solid line* shows the present numerical solution, and *circles* show the solution computed by Blyth et al. [19] for a single fluid

4.2 Results

At zero Reynolds number, the solution is periodic and the reduced thread radius, $s(t)$, oscillates about a mean position regardless of the initial condition, $s_0 = s(0)$, as discussed in Sect. 2. At finite Reynolds number, $R > 0$, there exists a cut-off point for the initial condition, s_0^*, which divides the long-term behaviour into two types. In type (*i*), when $s_0 < s_0^*$, the inner fluid thread shrinks towards a cylinder of vanishing radius. In (*ii*), when $s_0 > s_0^*$, the outer fluid layer thins to an annulus of small thickness. For the special value $s_0 = s_0^*$, the reduced thread radius oscillates about a mean position, corresponding to a time periodic solution of the Navier–Stokes equations. The size of s_0^* depends on the parameter values. Under certain parametric conditions, only type (*i*) behaviour is found, meaning that $s_0^* \geq 1$; under different conditions, only type (*ii*) behaviour is found, meaning that $s_0^* \leq 0$.

In Fig. 8a we plot $s(t)$ against time at $R = 20$ for the case of moderate wall vibration, $\Delta = 0.2$, when the inner fluid layer is more viscous than the outer layer, with $\lambda = 0.5$. Solutions are shown for different initial conditions, $s_0 = s(0)$. The curves which depart from $s_0 = 0.1$ and 0.3 approach zero as time increases, corresponding to an increasingly slender thread and thick annular layer. When $s_0 = 0.4$, 0.5, or 0.9, the outer fluid layer shrinks to a thin annular film. In either case, the rate of change of the reduced thread radius slows as time progresses. Detailed calculations reveal that the cut-off value in the present case lies in the range $0.398 < s_0^* < 0.399$. In particular, when $\mathrm{d}t = 0.005$ and $N = 100$, we find $s_0 = 0.39863$, and when $\mathrm{d}t = 0.001$ and $N = 200$, we find $s_0 = 0.39817$.

The effect of varying the Reynolds number is illustrated in Fig. 8b for the case $\lambda = 0.5$ and $\Delta = 0.2$. For each simulation, the initial condition is taken to be the critical value, s_0^*, for $R = 20$. The curve for $R = 20$ oscillates about a mean position, corresponding to a periodic solution. The period is equal to T, the period of the pulsation of the wall. When $R = 15$, $s(t)$ tends to increase, meaning that the cut-off point at this Reynolds number is smaller than that for $R = 20$. When $R = 25$, $s(t)$ tends to decrease, meaning that the cut-off point at this Reynolds number is larger than that for $R = 20$. Careful calculations show that when $R = 25$ the cut-off point lies somewhere between 0.531 and 0.532. This demonstrates that the cut-off point increases with increasing Reynolds number. Calculations for different wall amplitudes, Δ, exhibit generically similar type (*i*) or type (*ii*) long-term behaviour.

The general dependence on Reynolds number of the cut-off value s_0^* when $\lambda = 0.5$ and $\Delta = 0.2$ is shown in Fig. 9a. Evidently the cut-off value decreases with decreasing Reynolds number. The curve intercepts the horizontal axis at $R \approx 15.5$, so that only type (*ii*) behaviour is found at smaller Reynolds number. We have not been able to find any parameter values for which s_0^* reaches unity. The effect of the viscosity ratio on the cut-off point is shown in Fig. 9b for $\Delta = 0.2$ and the two values of the Reynolds number, $R = 20$ and $R = 10$. Increasing the viscosity ratio

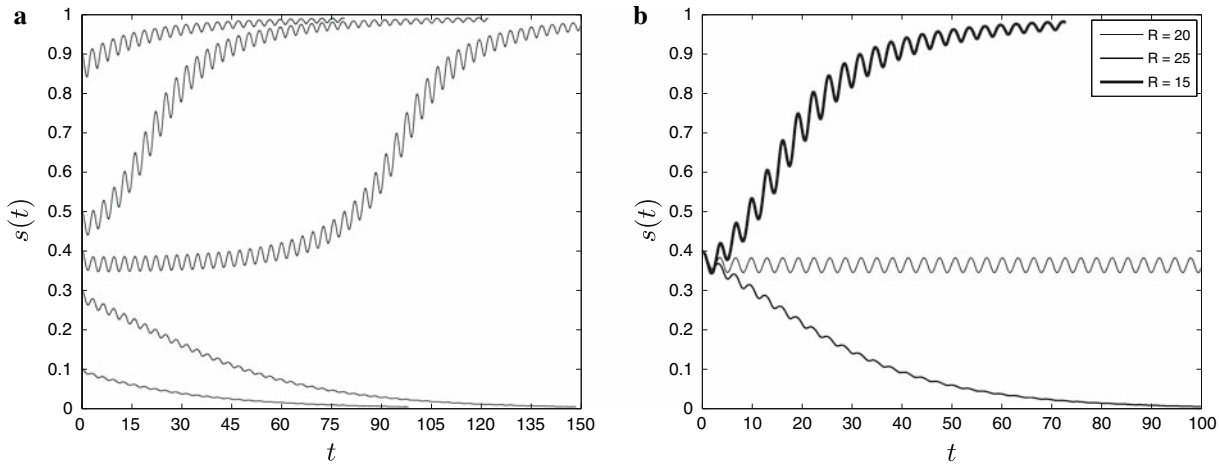

Fig. 8 **a** The reduced thread radius, $s(t)$, against time when $s_0 = 0.1, 0.3, 0.4, 0.5$ and 0.9, for the case $\lambda = 0.5$, $\Delta = 0.2$ and $R = 20$. **b** $s(t)$ against time for the case $R = 15$, 20 and 25 when $\lambda = 0.5$ and $\Delta = 0.2$. The initial condition is $s_0 = s_0^*$ for $R = 20$

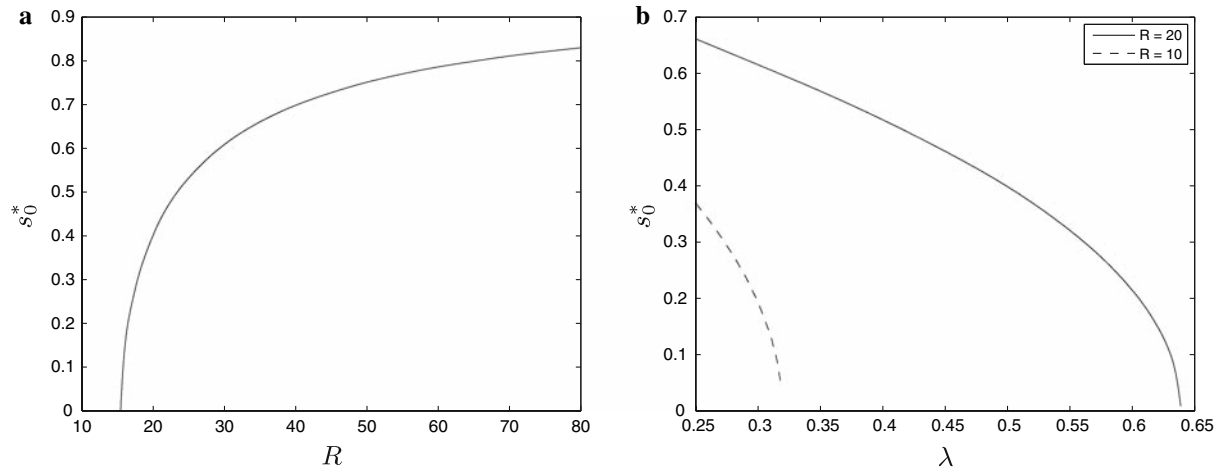

Fig. 9 **a** Variation of the cut-off point, s_0^*, with the Reynolds number, R, when $\lambda = 0.5$ and $\Delta = 0.2$. **b** Variation of the cut-off value, s_0^*, with the viscosity ratio λ, when $\Delta = 0.2$ and $R = 20$ (*solid line*) and $R = 10$ (*broken line*)

tends to lower the value of s_0^*, reducing it to zero at a critical value, λ_c, which depends on the Reynolds number. For $R = 20$, we estimate $\lambda_c \approx 0.64$ and for $R = 10$ we estimate $\lambda_c \approx 0.32$. Consequently, lowering the Reynolds number lowers the critical viscosity ratio. The effect of the wall amplitude Δ on the cut-off point s_0^* is shown in Fig. 10a for the case $R = 20$ and $\lambda = 0.5$. The cut-off value increases monotonically for pulsations of increasing amplitude.

To eliminate the oscillations and illustrate the average drift of the reduced thread radius during a simulation, we define the mean thread radius at a given time instant,

$$\bar{s}(t) \equiv \frac{1}{T}\int_t^{t+T} s(\tau)\,\mathrm{d}\tau. \tag{4.17}$$

This is plotted in Fig. 10b for the Reynolds numbers 0.1, 1, 5, 10, 15 and 20. In all cases, the calculations were initiated from the cut-off value s_0^* for $R = 20$. The trace of the mean thread radius for $R = 20$ is a horizontal line corresponding to a periodic solution. Because of the initial condition, all solutions for $R < 20$ correspond to type (*ii*) solutions in which the thickness of the outer layer tends to thin (see Fig. 9a). The rate at which the outer thread thins during the simulation first increases as the Reynolds number is lowered to $R = 10$. Thereafter, as the Reynolds

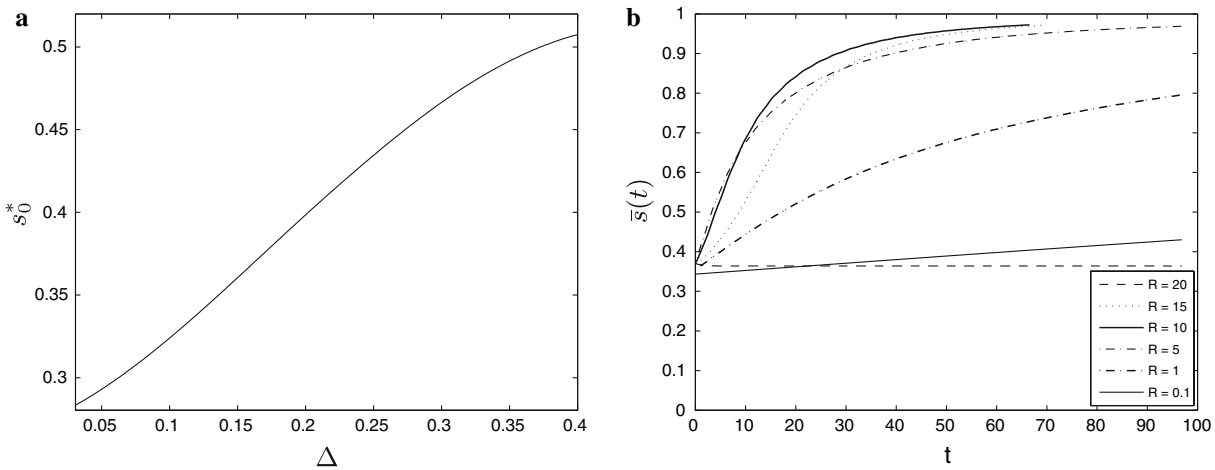

Fig. 10 **a** Dependence of the cut-off point, s_0^*, on the wall amplitude, Δ for the case $\lambda = 0.5$ and $R = 20$. **b** The mean value $\bar{s}(t)$ for, $R = 20$, 15, 10, 5, 1, and 0.1, when $\lambda = 0.5$ and $\Delta = 0.2$. The initial condition is $s_0 = s_0^*$ for $R = 20$

number is reduced below 10, the outer thread thins more slowly. When $R = 0.1$, the mean thread radius changes by only around 25.25% from $t = 0$ up to $t = 100$. As $R \to 0$, the rate at which the outer layer thins approaches zero. In the limiting case of Stokes flow, $R = 0$, the solution is periodic and the trace of $\bar{s}(t)$, is again a horizontal line.

5 Discussion

We have considered the flow of a viscous thread surrounded by an annular viscous layer inside a cylindrical pipe whose radius is a periodic function of time. For zero Reynolds number flow, we derived an exact solution in which the interface between the fluids is a circular cylinder whose radius varies periodically with the same period as the wall motion. In the analogous two dimensional channel flow studied by Blyth [18], it is possible to choose the initial interface location so that the thickness ratio of the two fluid layers remains constant throughout the motion. This is not possible in the axisymmetric problem, and the layer thickness ratio varies periodically regardless of its initial location.

We performed a linear stability analysis for Stokes flow and computed the growth rates of infinitesimal disturbances. For a static configuration with the wall stationary, the thread is unstable to disturbances with wavelength longer than the thread circumference according to Rayleigh's criterion. When the fluid in the annular film is less viscous than the fluid in the thread, the pulsations increase the growth rate of long wavelength disturbances for a moderate initial thread radius, but decrease the growth of longwave disturbances when the annular layer is thin. However, when the fluid in the thread is much less viscous than that in the annular film, and the annular film is thin, the pulsations tend to promote the growth of longwave disturbances. This observation may have implications for flow in the lungs, where longwave disturbances to the thin mucus lining on the inside of the airways are expected ([3, 22]). For a moderate initial thread radius, the pulsations reduce the critical wavenumber for instability to below the classical Rayleigh threshold. When the annular layer is thin, the critical wavenumber first drops to a minimum and is then raised to above the Rayleigh threshold as the amplitude of the pulsations increases. Also, for a moderate initial thread radius, the pulsations tend to lower the growth rate of the most unstable wave, so that for large wall amplitudes the pulsations have a stabilising influence on the flow.

In the second part of the paper, we computed the flow at arbitrary Reynolds number on the assumption that the interface between the two fluids is a circular cylinder throughout the motion. For all cases computed, the flow is synchronous with the forcing wall motion. For general parameter values, there exists a cut-off value of the inital thread radius which divides the subsequent flow into two categories of long-term behaviour. Either the ratio between

the thread radius and the wall radius tends towards a unit value, meaning that the outer layer tends to thin, or else the ratio tends to zero, in which case the inner thread tends to shrink. If the initial thread radius corresponds to the cut-off value, the solution is time-periodic and the ratio between the thread radius and the wall radius oscillates about a non-zero mean value. Extensive computations revealed that the cut-off value decreases with Reynolds number. Below a threshold value of the Reynolds number, only the first type of behaviour is observed in which the annular outer layer tends to thin as the flow evolves. The cut-off number is also sensitive to the viscosity ratio and to the amplitude of the pulsations. By either decreasing the viscosity ratio or increasing the pulsation amplitude, the cut-off value is increased, thereby widening the range of initial conditions for which the inner thread will tend to shrink during the subsequent motion.

In conclusion, at zero Reynolds number pulsations may either increase or decrease the growth rate of the most dangerous disturbance, depending on the dimensionless initial thread radius. The stability of the flow at finite Reynolds number will form the subject of a future investigation.

References

1. Pal A, Brasseur JG, Abrahamsson B (2007) A stomach road or "Magenstrasse" for gastric emptying. J Biomechanics 40:1202–1210
2. Johnson M, Kamm RD, Shapiro LW, Pedley TJ (1991) The nonlinear growth of surface-tension-driven instabilities of a thin annular film. J Fluid Mech 233:141–156
3. Halpern D, Grotberg JB (1992) Fluid-elastic instabilities of liquid-lined flexible tubes. J Fluid Mech 244:615–632
4. Rayleigh JWS (1879) On the capillary phenomena of jets. Appendix I. Proc R Soc A 29:71–97
5. Rayleigh JWS (1892) On the instability of a cylinder of viscous liquid under capillary force. Philos Magn 34:145–154
6. Eggers J (1997) Nonlinear dynamics and breakup of free-surface flows. Rev Mod Phys 69(3):865–929
7. Weber ZZ (1931) Zum Zerfall eines Flussigkeitsstrahles. Z Math Mech 11:136–154
8. Tomotika S (1935) On the instability of a cylindrical thread of a viscous liquid surrounded by another viscous fluid. Proc R Soc A 150:322–337
9. Goren SL (1962) The instability of an annular thread of fluid. J Fluid Mech 12(2):309–319
10. Hammond PS (1983) Nonlinear adjustment of a thin annular film of viscous fluid surrounding a thread of another within a circular cylindrical pipe. J Fluid Mech 137:363–384
11. Kwak S, Pozrikidis C (2001) Effect of surfactants on the instability of a liquid thread or annular layer Part I: Quiescent fluids. Int J Multiph Flow 27(1):1–37
12. Tomotika S (1936) Breaking up of a drop of viscous fluid immersed in another viscous fluid which is extending at a uniform rate. Proc R Soc A 153:302–318
13. Mikami T, Cox RG, Mason SG (1975) Breakup of extending liquid threads. Int J Multiph Flow 2(2):113–138
14. Kwak S, Fyrillas MM, Pozrikidis C (2001) Effect of surfactants on the instability of a liquid thread Part II: extensional flow. Int J Multiph Flow 27(1):39–60
15. Khakhar DV, Ottino JM (1987) Breakup of liquid threads in linear flows. Int J Multiph Flow 13(1):71–86
16. Halpern D, Grotberg JB (2003) Nonlinear saturation of the Rayleigh instability due to oscillatory flow in a liquid-lined tube. J Fluid Mech 492:251–270
17. Blyth MG, Pozrikidis C (2005) Effect of pulsations on the stability of a gas column. Theor Comput Fluid Dyn 19(1):23–37
18. Blyth MG (2007) Effect of pulsations on two-layer channel flow. J Eng Math 59:123–137
19. Blyth MG, Hall P, Papageorgiou DT (2003) Chaotic flows in pulsating cylindrical tubes: a class of exact Navier–Stokes solutions. J Fluid Mech 481:187–213
20. Pozrikidis C, Blyth MG (2004) Effect of stretching on interfacial stability. Acta Mechanica 170(3–4):149–162
21. Drazin PG (1992) Nonlinear systems. Cambridge University Press, Cambridge
22. Dragon CA, Grotberg JB (1991) Oscillatory flow and mass transport in a flexible tube. J Fluid Mech 231:135–155
23. Abramowitz M, Stegun IA (eds) (1965) Handbook of mathematical functions. Dover, New York
24. Pozrikidis C (2008) Numerical computation in science and engineering, 2nd ed. Oxford University Press, Oxford.
25. Hall P, Papageorgiou DT (1999) The onset of chaos in a class of Navier-Stokes solutions. J Fluid Mech 393:59–87